Acta Materialia 241 (2022) 118391

Contents lists available at ScienceDirect

Acta Materialia

journal homepage: www.elsevier.com/locate/actamat

Dendrite fragmentation mechanism under forced convection condition by rotating magnetic field during unidirectional solidification of AlSi7 alloy

Haijie Zhang[a], Menghuai Wu[a,*], Christian M.G. Rodrigues[a], Andreas Ludwig[a], Abdellah Kharicha[a], Arnold Rónaföldi[b], András Roósz[b], Zsolt Veres[c], Mária Svéda[b]

[a] Chair of simulation and modelling metallurgical processes, Metallurgy Department, Montanuniversitaet Leoben, Franz-Josef Street 18, 8700 Leoben, Austria
[b] MTA-ME Materials Science Research Group, ELKH, 3515 Miskolc Egyetemváros, Hungary
[c] University of Miskolc, Institute of Physical Metallurgy, Metal Forming and Nanotechnology, 3515 Miskolc Egyetemváros, Hungary

ARTICLE INFO

Article history:
Received 19 April 2022
Revised 20 September 2022
Accepted 26 September 2022
Available online 28 September 2022

Keywords:
Capillary-driven fragmentation
Flow-driven fragmentation
Re-melting, grain destruction
Macrosegregation
Microstructure

ABSTRACT

Forced convection and its effect on the microstructure evolution of an Al-7wt.%Si alloy during unidirectional solidification were studied experimentally. Under natural convection (gravity), columnar structures develop. However, under forced convection by activating a rotating magnetic field (RMF: 10 mT, 50 Hz), many equiaxed grains form in the half-radius region of the cylindrical sample, and a severe macrosegregation channel forms at the centre of the sample. Crystal fragmentation is regarded as the main source of equiaxed grains, but their formation mechanism and the fragment transport phenomenon are not fully understood. A mixed columnar-equiaxed solidification model with extension to consider two dendrite fragmentation mechanisms (capillary-driven and flow-driven), was used to reproduce the experiment with the objective to investigate the formation process of the microstructure and macrosegregation. Under the effect of the RMF-induced primary/secondary flow, the capillary-driven fragmentation mechanism, which is associated with dendrite coarsening, operates mainly in the peripheral region of the sample at a certain depth of the mushy zone. These fragments are difficult to be transported out of the (columnar dendritic) mushy zone. The flow-driven fragmentation mechanism associated with the interdendritic flow-induced re-melting of dendrites, operates mostly near the front of the mushy zone and/or around the central segregation channel. Some of these fragments can be transported out of the columnar tip region. In this case, a thin undercooled layer exists. Therefore, fragments can grow and become equiaxed grains. Some fragments are transported distally from the mushy zone into the bulk superheated region and are re-melted/destroyed there. The fragments, which continue to grow in the deep mushy zone or in the thin undercooled layer, are easily trapped by columnar dendrites, thereby competing with the growth of columnar dendrites to form a mixed columnar-equiaxed structure or even leading to a columnar-to-equiaxed transition.

1. Introduction

Dendrite fragmentation, i.e., the detachment of dendrite arms from a main dendrite stem, is considered as an important potential mechanism for the origin of equiaxed grains during alloy solidification [1,2]. Some fragments that are transported out of the columnar dendritic mushy zone after their formation either survive or are re-melted in the bulk melt region based on the local superheat condition. The fragments that survive may continue to grow into equiaxed grains and even lead to a columnar-to-equiaxed transition (CET) [3,4]. Formation of equiaxed crystals and CET are desirable for many castings [5,6]; however, the formation of such fragments, named stray/spurious grains, is detrimental to the quality of castings in the production of single-crystal turbine blades [7,8].

Despite the significance of this subject and research efforts in this field, information on crystal fragmentation is still limited and even controversial. Jackson et al. [9] first reported the re-melting induced fragmentation mechanism, i.e., local fluctuation of thermal and/or solute fields in the interdendritic region causing re-melting of the dendrite roots and consequently, leading to the formation of fragments. Because the detachment of sidearms by re-melting is a

* Corresponding author.
E-mail address: menghuai.wu@unileoben.ac.at (M. Wu).

https://doi.org/10.1016/j.actamat.2022.118391

part of the coarsening process and coarsening is strongly related to capillarity effect of the local dendrite morphology (curvature of solid-liquid interface) [10–14], this mechanism is later named capillary-driven fragmentation [11,13]. The corresponding process is further confirmed by recent *in situ* observations of solidification experiments on metal alloys [12,15–19]. The interdendritic flow also plays an important role in fragmentation [2,17,20–23]. For example, when an alloy solidifies under a forced flow condition, the fragmentation rate/frequency increases [20]. Note that flow exerts a shear force on the solidifying dendrite. This may cause mechanical fractures of side branches. Such mechanical fractures were once believed to be another mechanism for fragmentation [24,25]. However, this view has been rejected by many researchers. Several experiments have indicated that a certain delay from the start of the stirring to the onset of fragments is required [9,20,26]. This delay cannot be explained by mechanical fracturing. Based on a theoretical analysis [27], it has been proven that, under a strong liquid flow condition (0.01 m/s), the shear force exerted on the dendrite root does not reach 1% of its yield stress at that temperature.

In addition to experimental studies, numerical approaches such as the phase-field method have been used to model dendrite evolution and potential fragmentation [11,12,28–30]. The phase field method is indeed a proper approach to study the phenomena associated with dendrite evolution by tracking the dendrite fragmentation precisely; however, it is limited to the microscopic scale with a few dendrites. To manage billions of fragments and their transport at an engineering casting scale, a volume-average-based solidification model is required [31–35]. Fragmentation parameters (frequency N_{frag} and initial size $d^0_{\text{e,frag}}$), which cannot be directly calculated using the volume-average model, must be described using a sub-model. The volume-average model can act as a bridge between the fragmentation sub-model and global solidification/melting model that considers the transport of solute, energy, and fragments, so that an as-cast structure can be predicted.

Experimental studies have been used to estimate the fragmentation frequency, N_{frag}, based on optical observation using transparent analogue alloys or synchrotron X-ray radiographical investigations with real metal alloys [2,12,16,20,26]. For example, based on alloy compositions, N_{frag} (m−3s−1) was estimated to be 0.5 × 109 for Al-15 wt.%Cu [2,20], 0.28 × 109 for Al-20 wt.%Cu [16], and 2.83 × 109 for Al-30 wt.%Cu [16]. When pulsed electromagnetic fields are applied, N_{frag} increases significantly [20]. As the aforementioned counts were estimated optically, only fragments with a size of the order of secondary dendrite arms could be recognized. Hence, the value of N_{frag} might have been underestimated. The fragmentation rate for a steel casting was also estimated using 'fitting' parameters to match the experimental results of the as-cast structure [36]. A hypothesis was designed that stirring molten steel (natural convection) prior to the solidification front would result in seeding a liquid with dendritic fragments. These fragments were assumed to be eroded from the columnar front with fragment flux N_{flux} (m−2s−1) once a certain condition (a threshold of local thermal gradient) was fulfilled. This surface injection model for N_{flux} at the columnar front was later used in a volume-average solidification model to simulate an as-cast structure [37]. Such experiments or experiment-based methods provide valuable information on the magnitudes of N_{frag} (or N_{flux}) and $d^0_{\text{e,frag}}$. Unfortunately, the limited experimental data do not allow to set a sub-model that can correlate N_{frag} (or N_{flux}) and $d^0_{\text{e,frag}}$ with solidification parameters.

Therefore, alternative approaches have been explored. It is known from Flemings' local re-melting theory [38] that a flow in the direction of growth of primary columnar dendrites in the mushy zone promotes re-melting. On this base, an onset criterion for the flow-remelting-induced fragmentation was suggested by Campanella et al. [39] to analyse the potential occurrence of fragmentation. As a step further, the current authors proposed a flow-driven fragmentation formulation (sub-model) to quantify the relation between N_{frag} and flow [40]. The N_{frag} is assumed to be proportional to $-\gamma \cdot (\vec{u}_\ell - \vec{u}_c) \cdot \nabla c_\ell$, where $(\vec{u}_\ell - \vec{u}_c)$ is the relative velocity between the melt and columnar dendrites and ∇c_ℓ is the solute concentration gradient of the interdendritic melt. A fragmentation coefficient γ was introduced to consider other unknown contribution factors. This sub-model was implemented in a volume-average solidification model to reproduce the as-cast structures of an Sn-10 wt.%Pb alloy of a laboratory benchmark [41] and steel of an engineering continuous casting [42]. The value of γ was obtained via a numerical parametric study. Recently, Cool and Voorhees proposed another expression to estimate N_{frag} based on an isotherm coarsening experiment under the microgravity condition aboard the International Space Station (ISS) [12]. Statistically, the N_{frag} could be expressed as a function of the characteristic length scale of dendrites (solid-liquid interfacial density S_V). This expression was valid for the pure diffusive and isotherm condition, but the current authors extended it to solidification conditions [13]. Also, a more general coarsening law based on S_V was considered [28]. This capillary-driven fragmentation model has been implemented in a volume-average solidification model to reproduce a laboratory experiment on the NH_4C1-H_2O alloy [43]. However, some material-related coefficients for the coarsening law (Chapter 3.1) need to be fitted through a parametric study. The above two fragmentation sub-models, namely, flow-driven and capillary-driven models, were derived from different theoretical backgrounds. Although the former highlights the flow-induced remelting effect, it fails to explain the crystal morphology, growth/remelting kinetics, and their impact on fragmentation. The latter model considers more morphological and kinetic effects but ignores the flow impact.

In this study, both flow-driven and capillary-driven sub-models were combined and compared based on a unidirectional solidification experiment on an Al-7wt.%Si alloy. Some *in situ* experiments have observed both fragmentation mechanisms would operate simultaneously [15]. Both sub-models were implemented in a mixed columnar-equiaxed solidification model. The first objective of this study was to reproduce the unidirectional experiments. The second objective was to analyse the evolution of the as-cast structure by considering crystal fragmentation based on above two mechanisms and the transport and growth/re-melting of crystal fragments.

2. Brief description of the experiment

A unidirectional solidification experiment on the Al-7.0wt.%Si alloy was performed in a Bridgman-type furnace [44], depicted in Fig. 1**(a)**. The size of the cylindrical sample was 100.0 mm × ϕ8.0 mm. The temperature profiles during the solidification were monitored using thermocouples, Fig. 1**(b)**. The temperature gradient in the sample was 7.0 ± 0.5 K/mm and the withdrawal rate of the sample was 0.1 ± 0.02 mm/s. The furnace was equipped with a two-pole inductor to produce a rotating magnetic field (RMF). The function area of the RMF was significantly longer than the sample length.

The as-solidified sample was metallographically analysed and its vertical section is depicted in Fig. 2**(a)**. The first part of the sample (Part 1: first 40 mm) solidified under natural convection; the second part (Part 2: from 40 mm to 80 mm) solidified under RMF (B = 10 mT, f = 50 Hz); and the remaining part (Part 3: >80 mm) solidified under natural convection. In Part 1, the columnar grains dominate and their structure is slightly inclined towards the sample surface. In Part 2, the long and thin columnar grains continue to develop in the peripheral region, while they transform into stubby grains along the middle of the sample. The grains

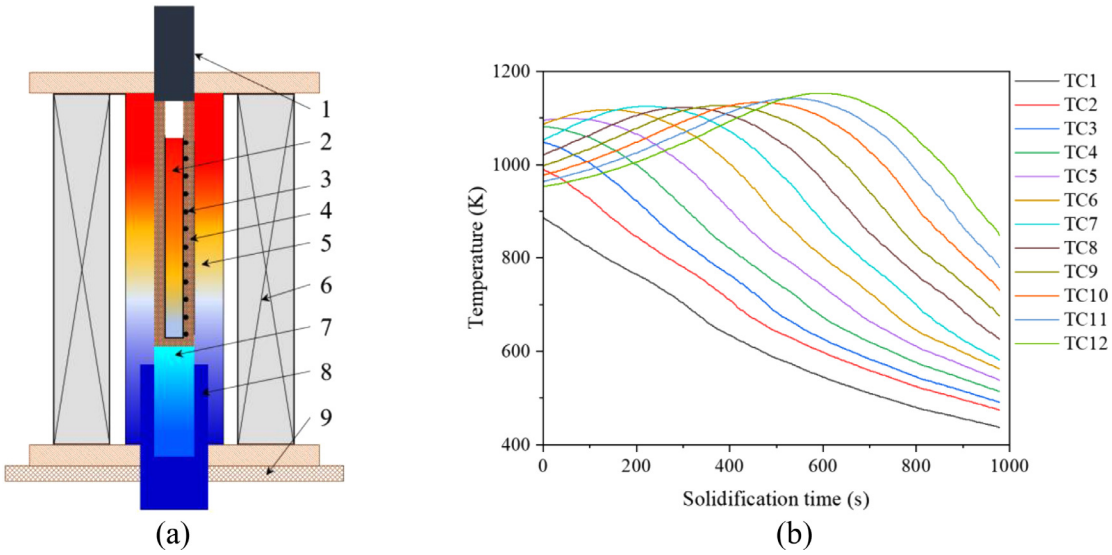

Fig. 1. (a) Schematic of unidirectional solidification facility: 1. step motor, 2. solidification sample, 3. thermocouples, 4. alumina crucible, 5. furnace with four heating zones, 6. RMF inductor, 7. copper cooling core, 8. cooling water, and 9. basement. (b) Evolution of temperature profiles.

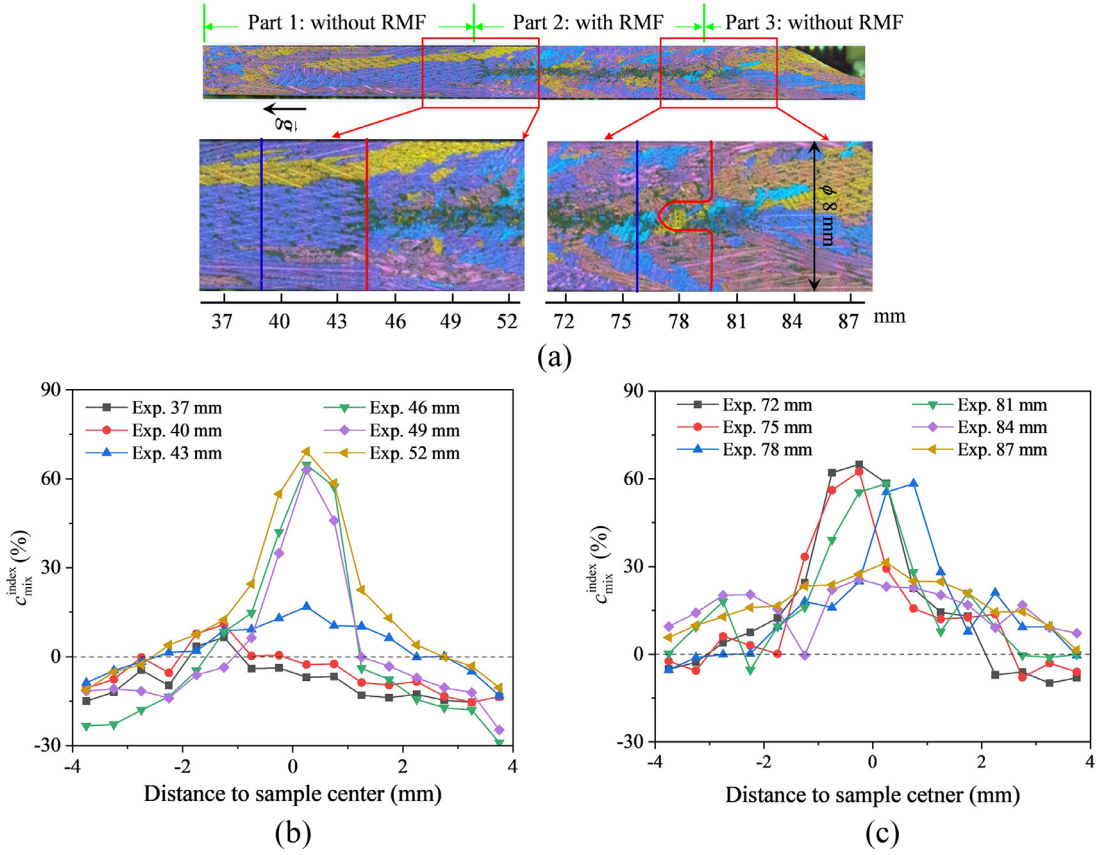

Fig. 2. Experimental result of the as-solidified Al-7.0wt.%Si sample. (a) Grain structure on the vertical section with two enlarged views before and after the activation of the RMF; the red/blue lines indicate the columnar tip-front/eutectic isotherm before and after the activation of the RMF. (b) and (c) Macrosegregation of Si ($c_{\mathrm{mix}}^{\mathrm{index}}$) profiles across the sample diameter at various heights near the regions before and after the activation of RMF, respectively.

are more inclined compared to Part 1. A severe macrosegregation channel forms in the sample centre, where dense fine equiaxed grains can be seen. After switching off the RMF in Part 3, the structure restores back to columnar dendrites and the segregation channel vanishes gradually. The cross-section morphology of the sample is discussed later in Fig. 6**(a)** and **(b)**.

The solute distribution (macrosegregation) was measured using the energy-dispersive X-ray spectroscopy (EDS) along the diameter of the sample. The size of the experimental measuring spot was large enough to "average" over the phases but small enough to resolve a concentration profile. The segregation profiles are depicted in Fig. 2**(b)** and **(c)**. The macrosegregation index is indicated as

$c_{\text{mix}}^{\text{index}}$, with $c_{\text{mix}}^{\text{index}} = (c_{\text{mix}} - c_0)/c_0 * 100\%$; where c_{mix} is the mixture concentration among columnar, equiaxed, and eutectic phases; and c_0 is the nominal composition of the alloy (7.0 wt.%). Corresponding to the segregation channel in Fig. 2**(a)**, in Part 2 with RMF, a high value of $c_{\text{mix}}^{\text{index}}$ is observed. In Parts 1 and 3 without RMF, although there are no segregation channels in the centre, a weak macrosegregation profile is still recognized across the section. The average concentration in Part 3 is evidently higher than that in Part 1, i.e., the solute progressively accumulates along the solidification direction.

3. Model description and simulation settings

A previously developed three-phase mixed-columnar-equiaxed solidification model [31,32,35] was used. The volume fractions for the three phases, namely, columnar f_c, equiaxed f_e and liquid f_ℓ, summed up to one. The columnar structure developed from the sample bottom and its tip front was traced based on the kinetics of the Lipton–Glicksman–Kurz model [45]. Heterogenous nucleation for equiaxed was ignored (no grain refiner); hence crystal fragmentation was regarded as the sole origin for equiaxed grains. Diffusion-governed growth kinetics was considered to calculate the solidification rate. The morphology of the columnar dendrite was simplified with a cylinder. The equiaxed dendrite was simplified as a spherical envelope with interdendritic melt and solid in it [46]. Thermodynamic equilibrium was assumed at the solid–liquid interface. The concentration difference between the thermodynamic equilibrium concentration of the liquid at the interface (c_ℓ^*) and the volume-average liquid concentration (c_ℓ) served as the driving force for solidification and melting. Re-melting of the as-formed/solidified equiaxed grains and columnar dendrites was considered. The growth of the equiaxed grains ahead of the columnar dendrite tips could cause CET [1,47]. In contrast, equiaxed grains, as-packed or as-captured by the columnar structure, could further develop into columnar structures, i.e., equiaxed-to-columnar-transition (ECT) occurred. The solidification model has been described elsewhere. Here, only the crystal fragmentation sub-models and grain destruction owing to re-melting are presented in detail.

Conservation of number density is solved considering the transport of equiaxed grains with the following equation

$$\frac{\partial}{\partial t} n_e + \nabla \cdot \left(\vec{u}_e n_e \right) = N_{\text{frag}}^{\text{capillary}} + N_{\text{frag}}^{\text{flow}} + N_{\text{des}}, \tag{1}$$

where n_e and $\vec{u}_e$ are the number density and velocity of equiaxed grains (or fragments), respectively; $N_{\text{frag}}^{\text{capillary}}$ and $N_{\text{frag}}^{\text{flow}}$ are the crystal fragment generation frequencies due to capillary-driven and flow-driven fragmentation mechanisms, respectively; and N_{des} is the destruction rate due to re-melting.

3.1. Capillary-driven fragmentation: $N_{\text{frag}}^{\text{capillary}}$

Competitive growth/re-melting due to the capillary effect of high-order dendrites in different locations leads to the formation of fragments in the deep mushy zone. Based on an isothermal coarsening experiment under a pure diffusive condition [12], Cool and Voorhees proposed a statistical expression to estimate $N_{\text{frag}}^{\text{capillary}}$:

$$N_{\text{frag}}^{\text{capillary}} = \frac{\mathrm{d}\left(a \cdot {S_V}^3\right)}{\mathrm{d}t}, \tag{2}$$

where a is an alloy-dependent constant and S_V is the solid-liquid interface area density calculated using the coarsening law [28]:

$$S_V = f_c (1 - f_c)^{\tilde{r}} \left(\left({S_{S0}}^{-1} \right)^3 + K_0 t_s \right)^{-1/3}, \tag{3}$$

where $\tilde{r}$, S_{S0}, and K_0 are alloy-dependent constants; and t_s (local solidification time) is the time from the first appearance of the local columnar structure. When solidification is dominated by dendrite growth, $N_{\text{frag}}^{\text{capillary}}$ is positive owing to an increase in S_V. When the solidification process is dominated by dendrite coarsening, the decrease in S_V causes $N_{\text{frag}}^{\text{capillary}}$ to be negative. Given that coarsening only occurs when the dendrite side branches have been well developed [9,12,28], 0.1 is taken as the minimal volume fraction of the columnar phase ($f_{\text{frag,oneset}}^{\text{capillary}}$) for the onset of fragmentation [13]. The initial diameter of fragments ($d_{\text{e,frag}}^0$) was estimated based on the Li and Beckermann formula [48]:

$$d_{\text{e,frag}}^0 = f_c \frac{1.6}{S_V}. \tag{4}$$

Given the above considerations, and assuming that all fragments become equiaxed crystals, the fragmentation-induced mass transfer from the columnar dendrites to equiaxed grains ($M_{\text{frag}}^{\text{capillary}}$) can be calculated as

$$M_{\text{frag}}^{\text{capillary}} = N_{\text{frag}}^{\text{capillary}} \left(\rho_e \frac{\pi}{6} \left(d_{\text{e,frag}}^0 \right)^3 \right). \tag{5}$$

3.2. Flow-driven fragmentation: $N_{\text{frag}}^{\text{flow}}$

The flow-driven fragmentation formulation [40] is described as follows:

$$N_{\text{frag}}^{\text{flow}} = \frac{M_{\text{frag}}^{\text{flow}}}{\frac{\pi}{6} \left(d_{\text{e,frag}}^0 \right)^3 \rho_e}, \tag{6}$$

with

$$M_{\text{frag}}^{\text{flow}} = -\gamma \cdot (\vec{u}_\ell - \vec{u}_c) \cdot \nabla c_\ell \cdot \rho_e \cdot f_c. \tag{7}$$

where $M_{\text{frag}}^{\text{flow}}$ denotes the mass transfer rate from the columnar to the equiaxed grains due to flow-driven fragmentation. All other unknown contributions to $M_{\text{frag}}^{\text{flow}}$ were assumed to be included in the coefficient γ, which is needed to be determined through parametric study. $d_{\text{e,frag}}^0$ was calculated using Eq. (4). Different from $N_{\text{frag}}^{\text{capillary}}$, $N_{\text{frag}}^{\text{flow}}$ activates only when the flow is presented and $(\vec{u}_\ell - \vec{u}_c) \cdot \nabla c_\ell < 0$.

3.3. Re-melting and grain destruction: N_{des}

As soon as the fragments are generated, they are termed as equiaxed grains. The equiaxed grains can be remelted if they are exposed to the superheated region. Re-melting of equiaxed grains causes not only a decrease in their size or volume but also leads to their final destruction, i.e., a decrease in the number density of equiaxed grains. Although only a volume-averaged grain diameter d_e can be computed in a volume-averaged method, it is natural to assume a statistical log-normal distribution of the grain diameter in each controlled volume [46]:

$$\frac{\mathrm{d}n_e}{\mathrm{d}x} = \frac{n_e}{\sqrt{2\pi}\sigma_d x} e^{-\frac{1}{2}\left(\frac{\ln(x) - \ln(\hat{d}_e)}{\sigma_d}\right)^2}, \tag{8}$$

where σ_d is the geometric standard deviation of the lognormal distribution; the dummy variable (x) corresponds to the grain diameter of various size classes; and $\hat{d}_e$ is the geometric mean. The destruction rate of the equiaxed grains by re-melting can be calculated using the following equations:

$$N_{\text{des}} = \nu_{\text{Re}} \cdot \left. \frac{d(n_e)}{d(x)} \right|_{x = d_{e,\text{critical}}}, \tag{9}$$

with

$$\nu_{\mathrm{Re}} = \frac{D_\ell}{l_\ell} \cdot \frac{(c_\ell^* - c_\ell)}{(1-k)c_\ell^*}, \tag{10}$$

where $d_{\mathrm{e,critical}}$ is the small critical grain diameter below which destruction occurs rapidly, k is the solute partition coefficient, and D_ℓ and l_ℓ are the solute diffusion coefficient and diffusion length in the liquid melt, respectively. When the equiaxed grains are remelted to smaller than $d_{\mathrm{e,critical}}$, they are eliminated from the system, i.e., they are destroyed. Parameter ν_{Re} is the reduction rate of the grain size due to re-melting. The modification on l_ℓ by the liquid convection was considered based on findings in an earlier study [49]. The momentum, species, and energy transfer during crystal fragmentation [40] and grain re-melting/destruction [32,46,50] were also treated carefully.

3.4. Simulation settings

The configuration of the simulation was identical with that of the experiment in Fig. 1 **(a)**. The calculation domain was limited to the solidification sample, and it was initiated with a uniform temperature (T_0) and solute concentration (c_0). The experimentally measured temperature (Fig. 1**(b)**) was used as the Dirichlet thermal boundary condition for the bottom, side, and top walls. No-slip flow boundary condition was applied for the side and bottom walls, whereas a free-slip boundary condition was used for the top wall. Both thermo-solutal convection and grain sedimentation were modelled using the Boussinesq approach. In a cylindrical coordinate system, $\vec{F}_{\mathrm{L}}$ is composed of $\vec{F}_\theta$, $\vec{F}_{\mathrm{r}}$, and $\vec{F}_{\mathrm{Z}}$. In the case of a uniform magnetic field rotating about a long cylinder, $\vec{F}_{\mathrm{Z}}$ is shown to be zero, and $\vec{F}_{\mathrm{r}}$ has a minor effect on the fluid flow when compared to $\vec{F}_\theta$ [51]. In this study, the RMF-induced Lorenz force $\vec{F}_\theta$ was calculated as follows:

$$\vec{F}_\theta = \frac{1}{2}\sigma\omega B^2 r\left(1 - \frac{u_\theta}{\omega r}\right)\vec{e}, \tag{11}$$

where σ is the electrical conductivity of the melt, $\omega = 2\pi f$ is the angular frequency of the magnetic field, B is the magnetic induction, u_θ represents the azimuthal velocity components of the liquid and equiaxed grains at radial coordinate r, and $\vec{e}$ is the tangential unit vector. To deal with the hydrodynamic interaction between phases, a simplified dendritic morphology is assumed for the equiaxed grains. The concept of 'equiaxed grain envelope' was employed. The solid 'dendrite' and the interdendritic melt are enclosed in the grain envelope. The ratio of the volume of solid 'dendrite' to the volume of the grain envelope is predefined as f_{si}. Material properties and other parameters are listed in Table 1.

To analyse the role of the two different fragmentation mechanisms in the structure formation, three cases were selected. Case I combined both flow-driven fragmentation and the capillary-driven fragmentation sub-models; whereas Case II considered flow-driven fragmentation sub-model and Case III considered capillary-driven fragmentation sub-model only. Both full 3D and 2D axis-symmetrical simulations were made; however, parametric studies were made in 2D. To verify the 2D calculations, a comparison between 2D and 3D calculations is presented in Section 4.5.

The mixed columnar-equiaxed solidification model was implemented in ANSYS FLUENT version 17.1. Simulations were made in transient and included all stages of solidification: Part 1 to Part 3. The time step used for this study was 0.002 s. For one time-step, it takes several to dozens of iterations to yield convergence. From time to time, the maximum iteration number was carefully checked, and a value of 20 is safe for most of the simulations. In this study, a maximum iteration of 30 was specified. However, when the normalized residuals of concentration, flow quantities, and continuity are below 10−4 and enthalpy quantities are below 10−7, the simulation can reach the next time step automatically. The typical mesh sizes were 2.5 × 10−4 m (3D) and 1.5 × 10−4 m (2D). One 3D simulation took approximately 5 weeks, whereas one 2D simulation took 1 week on a high-performance cluster (2.6 GHz, 28 cores).

4. Solidification sequence and structure formation

4.1. Solidification under thermo-solutal convection

Case I was taken as reference, and both flow-driven and capillary-driven fragmentation mechanisms were considered. Fig. 3 summarizes the solidification parameters at 380 s (Part 1). At this moment, only thermo-solutal convection operated. The schematic of Fig. 3**(a)** can assist in understanding the process. The liquid concentration c_ℓ is gradually increased in the mushy zone, Fig. 3**(b)**, until it reaches the eutectic concentration, $c_{\mathrm{eut}} = 12.6\%$. The weak inward flow ($\vec{u}_{\ell,\max} = 0.1\mathrm{mm/s}$), Fig. 3**(b)**, transports the solute-enriched liquid to the central area of the sample, causing the slightly-positive macrosegregation at the centre, Fig. 3**(c)**. Correspondingly, a weak negative macrosegregation forms near the lateral wall of the sample. As is evident in Fig. 3**(d)**, the largest constitutional undercooling of 4 K for ΔT ($\Delta T = T_f + m \cdot c_\ell - T$) appears just near the columnar tips. A thin layer (~0.7 mm) of undercooled liquid forms just above the columnar tip front. Fig. 3**(e)** depicts the columnar solidification rate ($M_{\ell\mathrm{c}}$: mass transfer rate from liquid to columnar). The larger the undercooling, the higher is the solidification rate. The volume fraction of columnar phase f_{c} is depicted in Fig. 3**(f)**. Below the eutectic isotherm (T_{eut}), the f_{c} (~49.6%) is almost uniformly distributed in the sample cross-section. The fragmentation rates due to $N_{\mathrm{frag}}^{\mathrm{capillary}}$ and $N_{\mathrm{frag}}^{\mathrm{flow}}$ are depicted in Fig. 3**(g)** and **(h)**, respectively. The $N_{\mathrm{frag}}^{\mathrm{capillary}}$ is approximately two orders of magnitude smaller than $N_{\mathrm{frag}}^{\mathrm{flow}}$. Furthermore, the capillary-driven fragments form mainly in the periphery of the sample (suspended green diamonds of the iso-surfaces of $N_{\mathrm{frag}}^{\mathrm{capillary}} = 2 \times 10^7$ in Fig. 3**(g)**), whereas the flow-driven fragments are mainly produced in the central area (bowl-shape area of the iso-surface of $N_{\mathrm{frag}}^{\mathrm{flow}} = 2 \times 10^7$, Fig. 3**(h)**). The negative $N_{\mathrm{frag}}^{\mathrm{capillary}}$ in the deep mushy zone indicates that some fragments vanish because of coarsening (coalescence or re-melting). With fragmentation, more equiaxed grains are generated in the central area, Fig. 3**(i)**. Only the fragments (equiaxed grains) near the tip front can move with a downward velocity, whereas the fragments produced deep in the mushy zone are trapped by columnar dendrites ($\vec{u}_{\mathrm{e}} \approx 0.0$). The fragments can continue to solidify in the undercooled interdendritic liquid, Fig. 3**(j)**, to form some traces of the equiaxed phase, Fig. 3**(k)** and **(l)**. The as-solidified structure is dominated by columnar dendrites.

4.2. Solidification by activating RMF

RMF was activated at 400 s. A summary of solidification parameters at 414 s (Part 2) is presented in Fig. 4. A strong rotating flow ($\vec{u}_{\ell,\mathrm{rota}}$) was activated by the RMF, which also induced a secondary flow ($\vec{u}_{\ell,\mathrm{sec}}$) [54]. The RMF-induced secondary flow had a similar flow pattern as the thermo-solutal convection, but it was approximately two orders of magnitude stronger. Therefore, it led to the onset of a central segregation channel, depicted by the red region in Fig. 4**(b)**. Interestingly, the strong flow changed ΔT. An iso-surface of $\Delta T = 0.0$ is depicted in Fig. 4**(c)**. Owing to the accumulation of the solute at the centre, ΔT changed from positive (undercooled) to negative (superheated). It is evident from the inset-in Fig. 4**(c)** that the liquid is superheated ($\Delta T < 0.0$) above this mushroom-shaped iso-surface and is undercooled ($\Delta T > 0$) be-

Table 1
Material properties and other parameters.

Properties/parameters	Symbol	Units	Values	Refs
Thermophysical properties				
Specific heat (different phases)	$c_p^{\ell}, c_p^{e}, c_p^{c}$	$J{\cdot}Kg^{-1}{\cdot}K^{-1}$	1140.0	[52]
Latent heat	Δh_f	$J{\cdot}Kg^{-1}$	4.0×10^5	[52]
Diffusion coefficient (in liquid)	D_ℓ	$m^2{\cdot}s^{-1}$	6.45×10^{-9}	[52]
Thermal conductivity (different phases)	k_p^{ℓ}, k_p^{e}, k_p^{c}	$W{\cdot}m^{-1}{\cdot}K^{-1}$	100.0	[52]
Liquid thermal expansion coefficient	β_T	K^{-1}	-1.85×10^{-4}	[52]
Liquid solutal expansion coefficient	β_c	wt.% $^{-1}$	1.3×10^{-3}	[52]
Density (different phases)	$\rho_\ell, \rho_e, \rho_c$	$Kg{\cdot}m^{-3}$	2535.0	[52]
Density difference between solid and liquid	$\Delta\rho$	$Kg{\cdot}m^{-3}$	100.0	[52]
Viscosity	μ_ℓ	$Kg{\cdot}m^{-1}{\cdot}s^{-1}$	2.52×10^{-3}	[52]
Electrical conductivity	σ	$\Omega^{-1}m^{-1}$	3.24×10^6	[44]
Thermodynamic properties				
Eutectic temperature	T_{eut}	K	850.0	[52]
Liquidus slope	m	K·wt. $\%^{-1}$	−6.62	[52]
Equilibrium partition coefficient	k	-	0.13	[52]
Primary dendrite arm spacing	λ_1	μm	300.0	[44]
Gibbs–Thomson coefficient	Γ	m·K	2.41×10^{-7}	[52]
Melting point of pure solvent	T_f	K	935.5	[52]
Coarsening/fragmentation parameters				
Coarsening	$\tilde{r}$		0.25	[28]
constants	S_{S0}^{-1}	μm	2.46	[28]
	K_0	$\mu m^3/s$	23.5	[28]
Fragmentation	a	-	1.0×10^{-5}	[12]
constant/coefficient	γ	-	0.4	-
Other parameters				
Critical grain diameter for destruction	$d_{e,critical}$	μm	30.0	[46]
Solid fraction in the dendrite envelope	f_{si}	-	0.25	-
Initial concentrations	c_0	wt.%	7.0	-
Initial temperature	T_0	K	1100.0	-
Cooling rate	R	K/s	0.7	-
Temperature gradient	$\vec{G}$	K/m	7000.0	-
Magnetic induction	B	mT	10.0	-
Rotating frequency of magnetic field	f	Hz	50.0	-

*Superscripts and subscripts e, c, and ℓ indicate different phases.

low it. As marked by "A" in Fig. 4**(c)**, some area below the columnar tip front is changed to superheated. Right in this "A" area, re-melting of columnar phase ($M_{\ell c}$ = -1.0 Kg·m−3s−1), indicated by the blue spots in the inset-in Fig. 4**(d)**, is observed. The relatively strong RMF-induced secondary flow enhanced the columnar solidification in the peripheral region of the sample. The f_c is depicted in Fig. 4**(e)** and $N_{frag}^{capillary}$ is presented in Fig. 4**(f)**. Different from the case with only thermo-solutal convection, with RMF, the $N_{frag}^{capillary}$ is magnified by more than one order of magnitude and its formation position is more concentrated near the lateral surface of the sample. Remarkably, there is almost no fragment generated by this mechanism in the central area. On the contrary, a large N_{frag}^{flow} (>1010 m−3s−1) is observed at the centre, Fig. 4**(g)**. It is evident from the inset that most of the flow-driven fragments are generated just below the solidification front and around the central segregation channel. The N_{frag}^{flow} is two orders of magnitude larger than $N_{frag}^{capillary}$ and more equiaxed grains are generated in the central area, Fig. 4**(h)**. A maximal $M_{\ell e}$ (107.0 Kg·m−3s−1) is seen in the central area close to the solidification front in Fig. 4**(i)**. The equiaxed solidification (positive $M_{\ell e}$) ahead of the columnar tip front, just corresponding to the thin undercooled layer in Fig. 4**(c)**, reflects the fact that the crystal fragments brought ahead of the columnar tip front still have a chance to grow. As depicted in Fig. 4**(h)**, some equiaxed grains can be dragged out of the mushy zone and move with the liquid. Because the solid grains are denser than the liquid, the grains move upwards a little slower than the liquid, e.g., $|\vec{u}_{e,sec,max}| = 9.8(mm/s)$ and $|\vec{u}_{\ell,sec,max}| = 11.8(mm/s)$. The contour of $M_{\ell e}$ is presented in Fig. 4 **(i)**. The negative $M_{\ell e}$ within the white isoline of $M_{\ell e} = 0$ denotes the re-melting of equiaxed grains. In the superheated liquid, the equiaxed grains decrease in size by re-melting, as indicated by d_e in Fig. 4**(j)**, and then they are fully re-melted and disappear, Fig. 4**(k)**. Because of the high value of n_e near the central channel, d_e becomes small there. The role of RMF in f_e can be seen in Fig. 4**(l)**. The f_e has been increased from 1.0% to 4.1% in 14 s by activating the RMF.

4.3. Macrosegregation evolution under steady RMF

Fig. 5 illustrates the evolution of c_{mix}^{index} under steady RMF. Only the results in the mushy zone, which is confined between the isosurface of $T = T_{eut}$ and f_c= 0.01, are depicted in **Fig. 5(a)**. The direction of $\vec{u}_\ell$ is indicated by the black arrows. Just before the activation of RMF at 400 s, the columnar tip front ($f_c = 0.01$) is located at h = 39.2 mm. At that moment, $\vec{u}_\ell$ is so small (∼ 0.1 mm/s) that c_{mix}^{index} is negligible ($|c_{mix}^{index}| < 1\%$), Fig. 5 **(a1)**. By activating RMF, $\vec{u}_\ell$ is raised by two orders of magnitude. The solute-enriched liquid is rapidly transported to the central area, leading to the onset of the central segregation channel, Fig. 5**(a2)**. Owing to the difference in permeability, the interdendritic flow near the columnar tip is much easier than that in the deep mush. The central segregation channel (similar to a tube) forms mainly in the upper region (near the columnar tip) of the mushy zone by sucking the solute-enriched melt into it, Fig. 5**(a3)** and **(a4)**. After the eutectic reaction, c_{mix}^{index} across the sample diameter at various heights, as marked by hori-

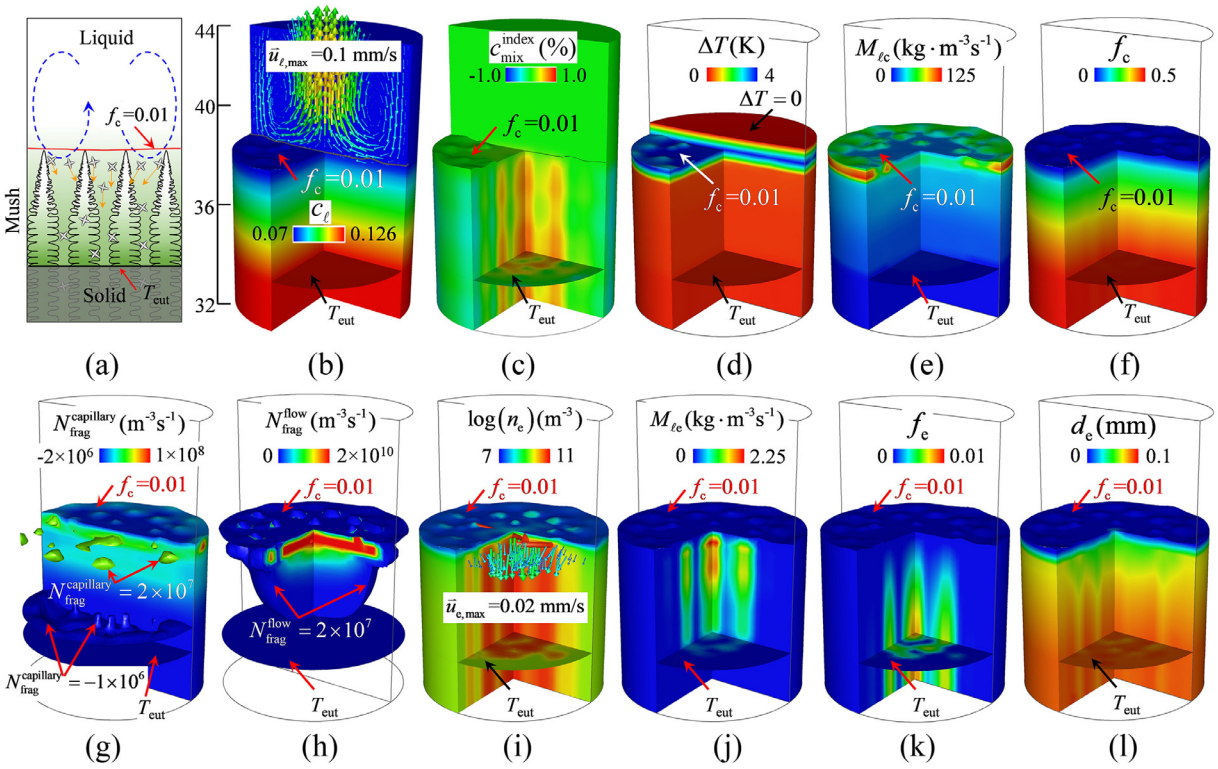

Fig. 3. Solidification under thermo-solutal convection at t = 380 s. (a) Schematic of solidification process; (b) concentration of melt c_ℓ overlaid by vectors of $\vec{u}_\ell$; (c) macrosegregation index c_{mix}^{index}; (d) undercooling ΔT; (e) solidification-induced mass transfer rate from liquid to columnar $M_{\ell c}$; (f) f_c; (g) fragmentation rate due to capillary-driven mechanism $N_{frag}^{capillary}$; (h) fragmentation rate due to flow-driven mechanism N_{frag}^{flow}; (i) log(n_e) overlaid by vectors of $\vec{u}_e$; (j) solidification-induced mass transfer rate from liquid to equiaxed phase $M_{\ell e}$; (k) f_e; and (l) size of equiaxed grains d_e.

zontal dash lines in Fig. 5**(c)**, is plotted in Fig. 5**(b)** to represent the dynamic evolution of c_{mix}^{index}. A reference line of $c_{mix}^{index} = 0$ is also added. All intersection points are marked by spheres of various colours. The corresponding radial coordinates of these spheres are overlaid as a function of the sample height in Fig. 5**(c)**. The spheres almost mark the outer profile of the 'fish-tail' segregation pattern. Therefore, a satisfactory simulation-experiment agreement, i.e., the fish-tail shape, is obtained.

4.4. Simulation-experiment comparison

Experiment-simulation comparisons of f_e on the cross-section are presented in Fig. 6**(a)** and **(b)**. In Part 1, few equiaxed grains ($f_e \approx 1\%$, numerically) can be seen. In Part 2 with RMF, the grains are considerably refined owing to the plentiful production of fragments. Based on the results of the simulation, f_e can reach up to 20%. The calculated c_{mix}^{index} at various heights across the sample diameter are compared with the experimentally measured values in Fig. 6**(c)**–**(f)**. The simulated onset of the central segregation channel and its termination by switching the RMF on/off are consistent with the experimental observation in Fig. 2**(a)**. A good experiment-simulation agreement is achieved.

The slight mismatch of the macrosegregation between the simulation results and the experimental measurements could be caused by the material properties which are assumed constant in this study. In addition, the assumptions and simplifications made in the volume-average-based solidification model, e.g., the flow-independent tip kinetics of Al dendrites, may also raise some discrepancies. Additionally, discrepancies could also be raised during the measurements. If the solute concentration was measured on another cross-section and/or along another mapping band, the experimental results will be more or less updated.

4.5. 3D simulations versus 2D simulations

The 3D and 2D simulations are compared in Fig. 7. The 2D simulation could successfully replicate the 3D simulation in terms of flow pattern and solidification sequence under both thermo-solutal convection and RMF conditions, but the flow intensity and c_{mix}^{index} were slightly overestimated. As depicted in Fig. 7**(a)**, a strong rotating flow of up to the magnitude of 38.6 mm/s was induced by activating the RMF. The imbalance in the dynamic pressure caused by the centrifugal force near the solidification front caused the secondary (poloidal) flow in Fig. 7**(b)** and **(c)**, which rotated and flowed to the solidification front before flowing upward along the centre line. The flow patterns of both simulations are similar. The major difference between the two flows is in their intensity. The 2D simulation apparently overestimated the maximum $|\vec{u}_\ell|$ (ca. 32.4%). This could lead to a slight overestimation of the segregation intensity and amount of the equiaxed phase. Note that the asymmetry of the as-solidified structure in Fig. 2**(a)**, observed experimentally, will never be reproduced in the 2D axis-symmetry.

5. Discussion

5.1. Capillary-driven fragmentation versus flow-driven fragmentation

To compare the two fragmentation mechanisms, the flow-driven fragmentation mechanism was simulated for Case II and the capillary-driven fragmentation mechanism was simulated for Case III. For Case I, simulations of both the mechanisms were used. The results are depicted in Fig. 8**(a)**–**(c)**. As a reference, the experimentally observed microstructure is depicted in Fig. 8**(d)**. The experiment indicated that most of the equiaxed grains were distributed

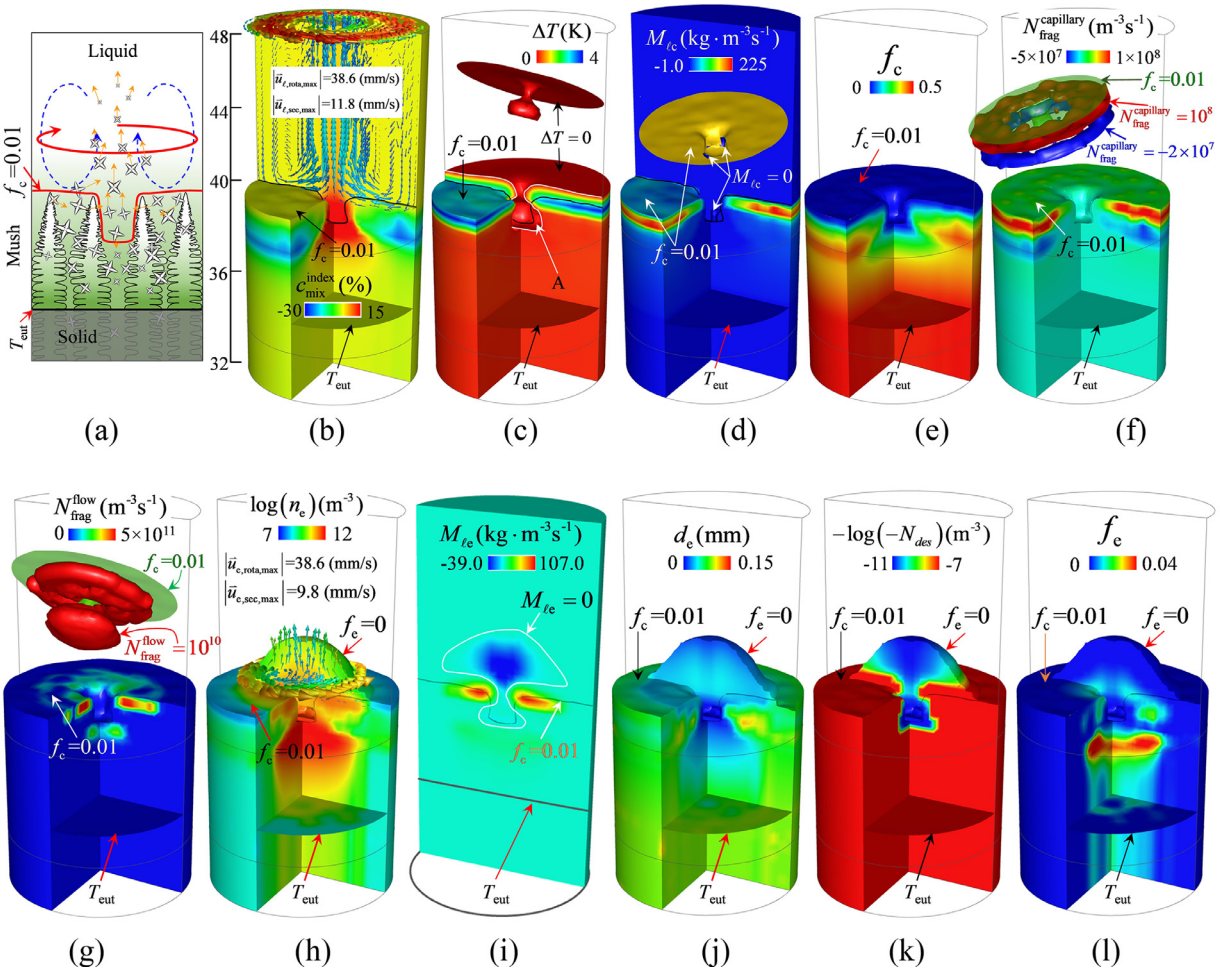

Fig. 4. Solidification at t = 414 s by activating RMF. (a) Schematic of solidification process; (b) c_{mix}^{index} overlaid by vectors of rotating velocity ($\vec{u}_{\ell,rota}$) on the top surface and the secondary flow ($\vec{u}_{\ell,sec}$) on vertical section; (c) ΔT; (d) $M_{\ell c}$; (e) f_c; (f) $N_{frag}^{capillary}$; (g) N_{frag}^{flow}; (h) log(n_e) overlaid by vectors of $\vec{u}_e$; (i) $M_{\ell e}$; (j) d_e; (k) -log(-N_{des}); and (l) f_e.

within half of the radius of the sample. From the experiment-simulation comparison, it could be concluded that the formation of the equiaxed grains was dominated by the flow-driven fragmentation, as shown by the $N_{frag}^{capillary}$ and N_{frag}^{flow} distributions in Fig. 4**(f)** and **(g)**, respectively. The fragments generated by the former are mostly concentrated near the sample surface and difficult to be transported by the interdendritic flow, whereas the fragments generated by the latter are concentrated near the central segregation channel and close to the columnar tip front. It is the fragments that are generated by the flow-driven fragmentation that are easily transported to the thin undercooled layer in front of the columnar tip. They grow as equiaxed grains and finally become captured by the columnar dendrites in the middle radius region of the sample.

One may argue that the calculated fragmentation phenomenon depends on fragmentation parameters (coefficient/constant) and their uncertainties would overshadow the above conclusion. Further parametric studies are presented in Section 5.2. Fragmentation parameters can only affect the fragmentation frequency (magnitude) but not the fragmentation locations. Regardless of the number of fragments created by the capillary-driven fragmentation mechanism, certain locations (near the sample surface) do not allow them to be transported out of the mushy zone. The RMF-induced flow in the experiment does not favour the capillary-driven fragmentation mechanism.

The current authors have previously conducted a similar comparison study based on another solidification experiment with aqueous ammonium chloride solution [43]. As schematically depicted in Fig. 9**(a)**, cooling and columnar growth start from the top of a solidification cell (4.2 × 2.8 × 1.27 cm3). Crystal fragments created in the columnar mushy zone can sediment downwards under natural convection and pile upwards from the bottom of the cell. The experiment measured the average columnar tip front (ACTF) position and average equiaxed pile-up front (AEPUF) position. Numerical simulations with the same solidification model, by considering either flow- or capillary-driven fragmentation mechanism, were performed. The results indicated that the capillary-driven fragmentation mechanism can better reproduce this experiment, **Fig. 9(b)**. The major differences in that experiment (aqueous ammonium chloride solution), in comparison with the present one, are that (1) the mushy zone of the aqueous ammonium chloride solution is highly porous (f_s < 0.2), and (2) the experiment configuration (vertical/downward solidification) is in favour of the transport of fragments. The fragments generated by either capillary- or flow-driven fragmentation can sediment downwards. Therefore, whether the capillary- or flow-driven fragmentation mechanism is dominant, the flow pattern (configuration of the solidification experiment) and alloy (porous or massive mushy zone) play critical role. This conclusion is supported by the observed different formation positions of fragments on Earth and aboard the ISS [15].

Recent *in situ* solidification observations [2,12,16–23,56–61] may provide further insight into the possible fragmentation mechanisms and their connections to the flow and alloy composi-

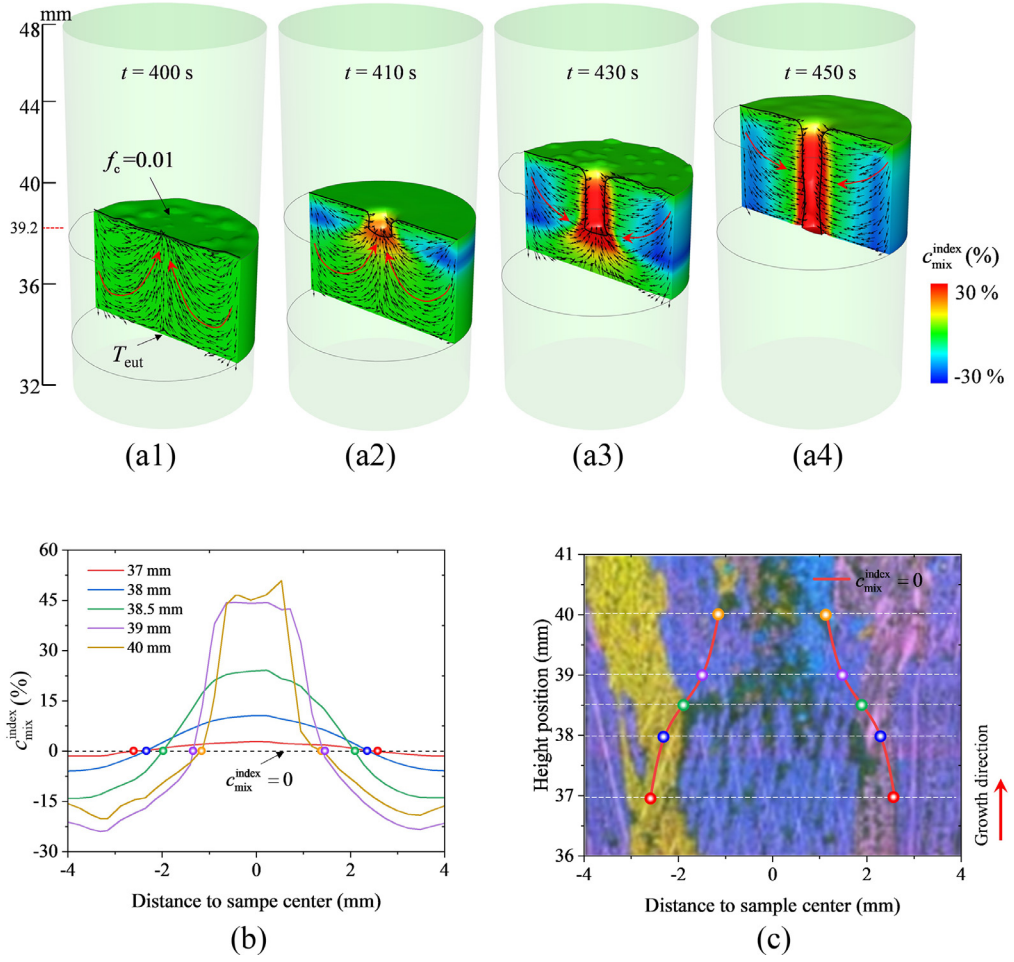

Fig. 5. Evolution of c_{mix}^{index} under steady RMF. (a1)–(a4) contours of c_{mix}^{index} in mushy zone (confined within f_c= 0.01 and $T = T_{eut}$) at 400, 410, 430, and 450 s. Black vectors indicate flow direction. (b) Simulated c_{mix}^{index} across the sample diameter of the as-solidified sample at various heights as marked by dash lines in (c). (c) Experimental result (metallograph) of the 'fish-tail' macrosegregation pattern by activating RMF.

tion. Under the microgravity condition [11,12,28,53], the fragmentation process is dominated by capillary-driven fragmentation. With strong flow [16–18,23,26], particularly under forced convection conditions [2], the flow-driven fragmentation abounds. Based on current studies, both capillary- and flow-driven fragmentation mechanisms should be included in the solidification model.

5.2. Fragmentation parameters

The calculated f_e in Case III (only the capillary-driven fragmentation), by varying the values of a, S_{S0}^{-1} and K_0, is presented in Fig. 10. When a is increased from 10−6 to 10−2, Fig. 10**(a)**, although the maximum value of f_e is raised by four orders of magnitude, the distribution of f_e is independent of a. Based on the experimental finding that only a small amount of equiaxed grains were generated in Parts 1 and 3 of the sample, a value of 10−5 is recommended for a in this alloy. Parameters S_{S0}^{-1} and K_0 impact the fragmentation frequency indirectly through the coarsening term in Eq. 3. When a large K_0 is used, the coarsening process starts late and most of the fragments are generated deep in the mush. Their subsequent growth is considerably suppressed by those as-developed columnar dendrites; therefore, the calculated f_e decreases with K_0, Fig. 10**(b)**. The role of S_{S0}^{-1} is similar to K_0. The coarsening rate will be fairly reduced if a large S_{S0}^{-1} is used. That is why f_e deceases with S_{S0}^{-1} (Fig. 10**(c)**). Because S_{S0}^{-1} directly affects the initial size of the formed fragments, an extremely large value of it is inappropriate. In this study, the current authors used the same values that were recommended for the Al-6wt.%Cu alloy [28] (namely, K_0 = 23.5 μm3·s−1 and S_{S0}^{-1} = 2.46 μm).

Simulations were performed based on Case II (only flow-driven fragmentation coefficient) to study the impact of γ on the calculated f_e, as depicted in Fig. 11. When γ is small (e.g., γ = 0.04), a maximum of 5.0% for f_e is found only in the 'fish-tail' region, above which f_e decreases to 1%. When γ is significantly large (e.g., γ = 4), too many equiaxed grains form before the activation of RMF, i.e., f_e = 10% in Part 1 of the sample, which is inconsistent with the experimental observations. A value of 0.4 is recommended for γ in the present study.

It has been known that the forced convection would adapt the tip velocity and the tip stability parameter for the dendrites. In the past decades, both experimental and theoretical studies have been tried to quantify the effect of liquid flow on dendrite tip selection [62-64]. However, it seems that there is no one well-established formulation available yet. In this study, the classical LGK model derived for the diffusive conditions was assumed to be validated for forced flow conditions. We believe this assumption may raise some discrepancies even though a very high temperature gradient was selected in the current case. If a well-established formulation for dendrite tip selection under forced flow conditions is available, numerical studies specific to this topic will be conducted.

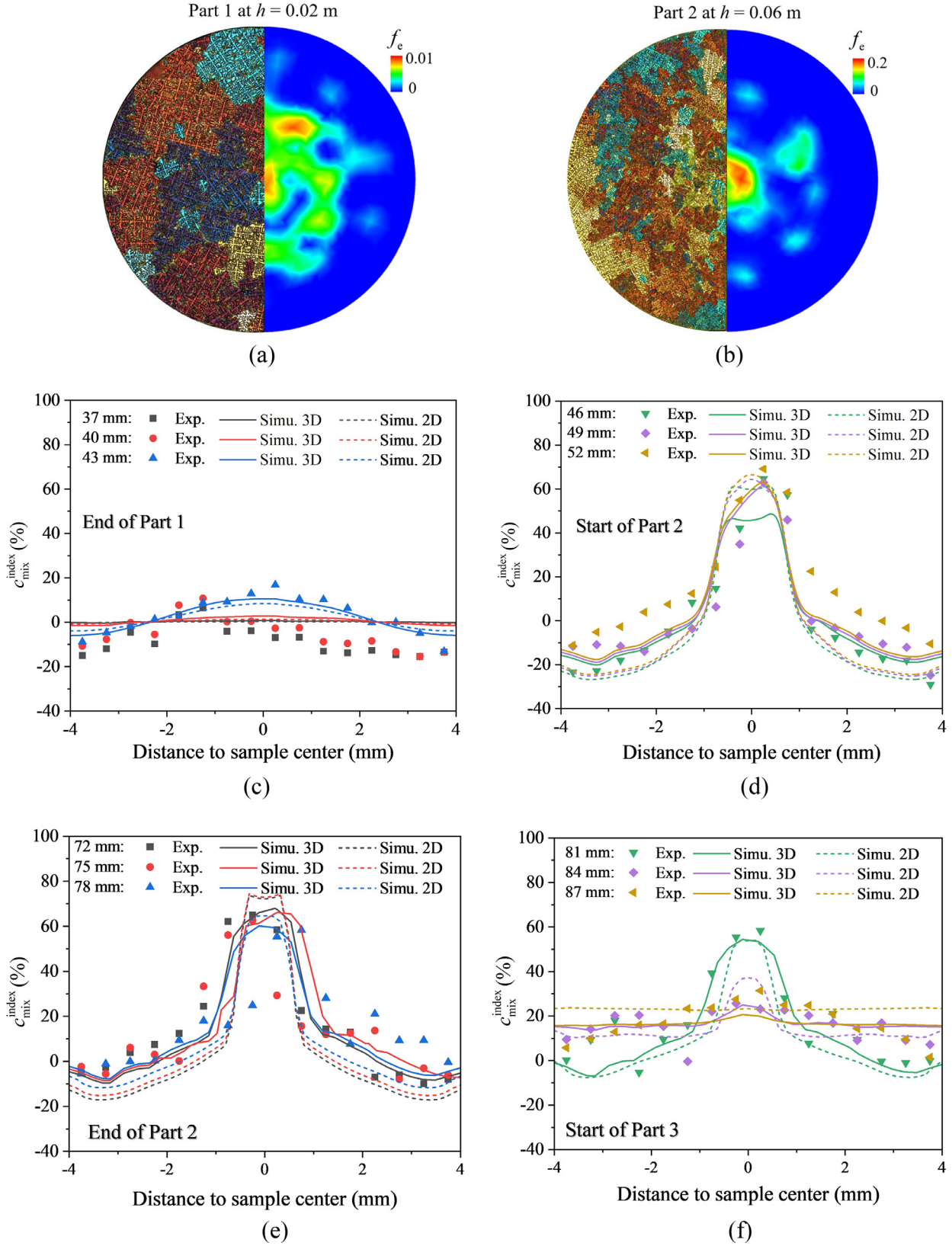

Fig. 6. Experiment-simulation comparison. As-solidified structure on the cross-section of the sample in (a) Part 1 without RMF and (b) Part 2 with RMF. (c)–(f) c_{mix}^{index} across the sample diameter at various heights in Parts 1, 2, and 3.

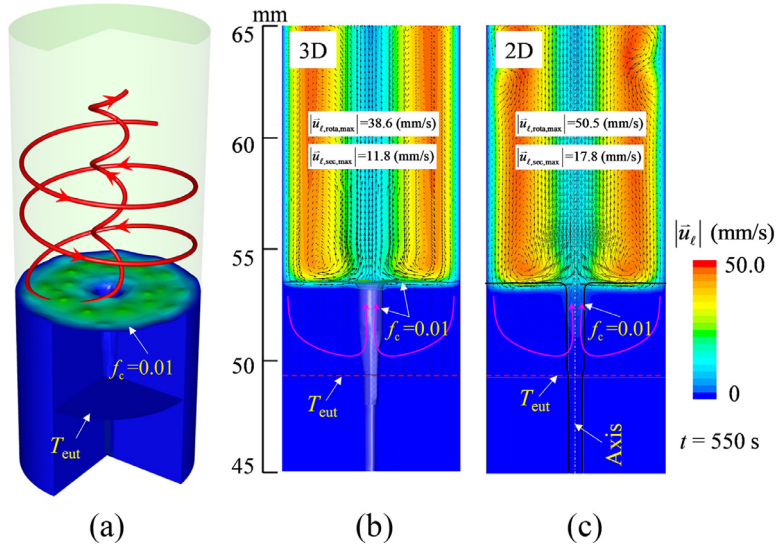

Fig. 7. Comparison between full 3D and 2D axisymmetric simulations at t = 550 s. (a) Contour of $|\vec{u}_\ell|$ overlaid by one streamline of $\vec{u}_\ell$; (b) and (c) contours of $|\vec{u}_\ell|$ on the vertical section of the sample overlaid by vectors of $\vec{u}_{\ell,\mathrm{sec}}$ in 3D and 2D cases, respectively.

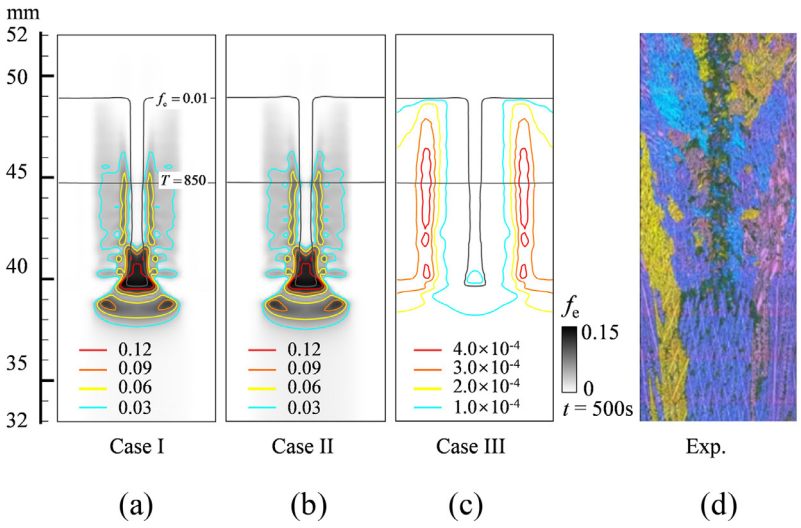

Fig. 8. Capillary-driven fragmentation vs. flow-driven fragmentation. (a)–(c) Contours of simulated f_e considering: (a) both flow-driven and capillary-driven mechanisms (Case I), (b) flow-driven fragmentation (Case II), and (c) and capillary-driven fragmentation (Case III). Isolines of f_e are overlaid in (a)–(c). (d) Experimentally observed structure on the vertical section of the sample.

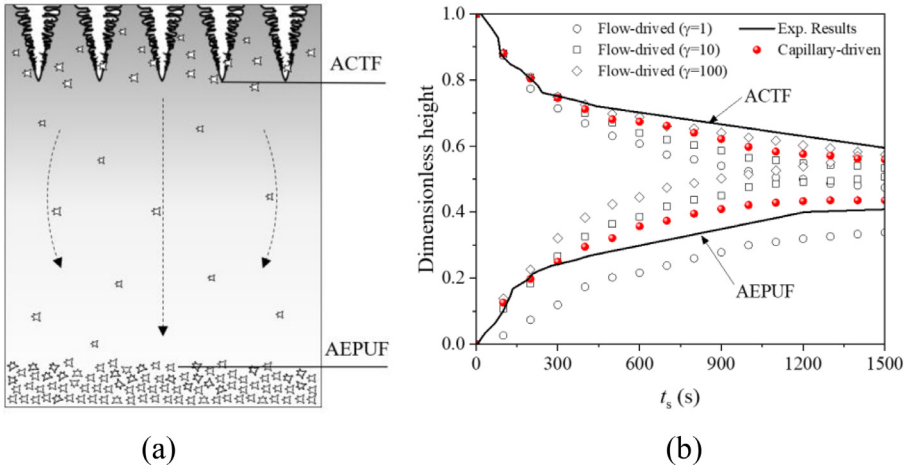

Fig. 9. Comparison between capillary- and flow-driven fragmentation sub-models based on a solidification experiment on aqueous ammonium chloride solution under natural convection [43,55]. (a) Schematic of solidification process. (b) Comparison of experimental and modelling results.

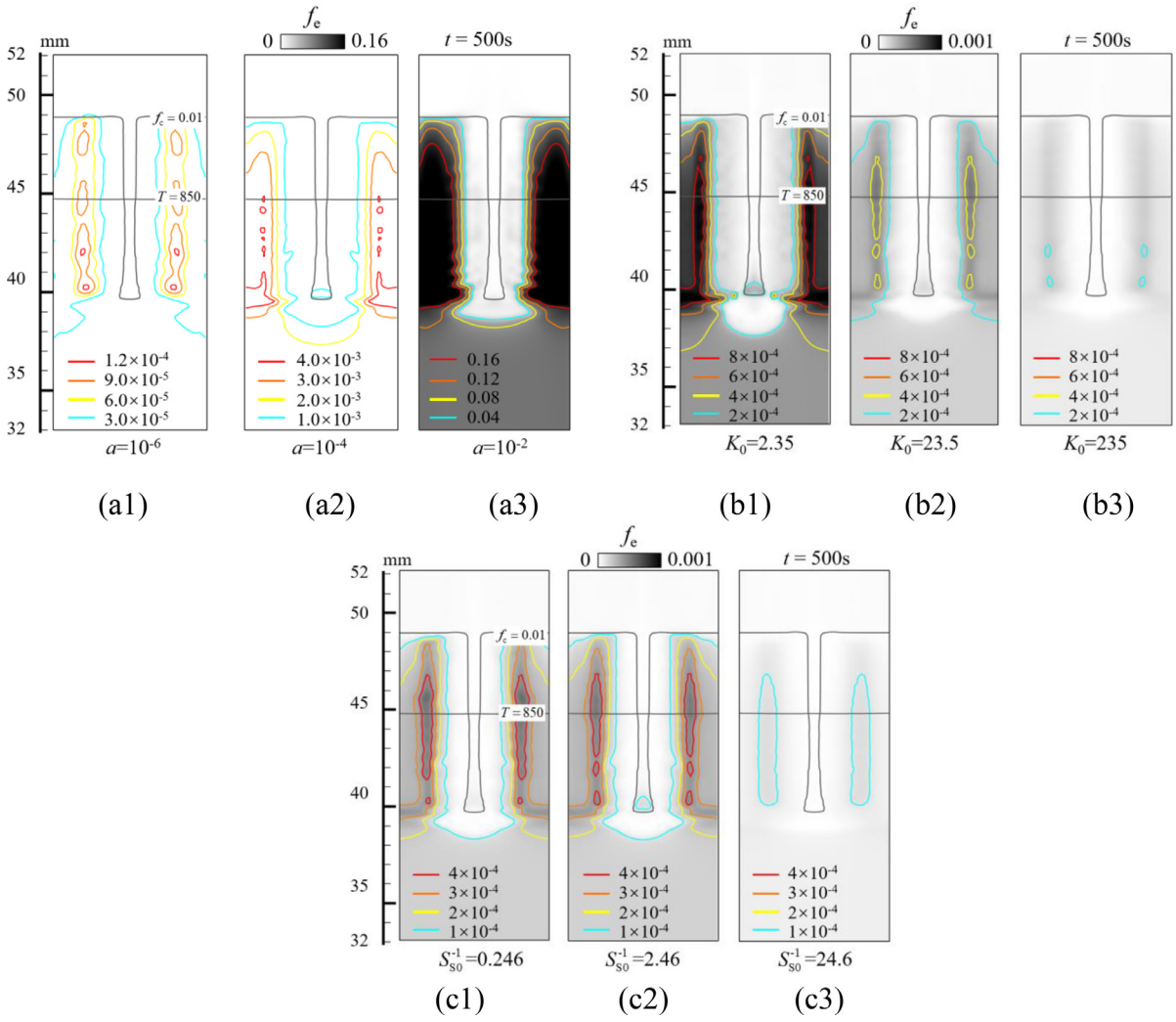

Fig. 10. Parametric study on capillary-driven fragmentation model. (a)–(c): Contours to display the effects of a, K_0, and S_{S0} on f_e. Isolines of f_e are overlaid. The values of variables outside each parametric study were taken from Table 1.

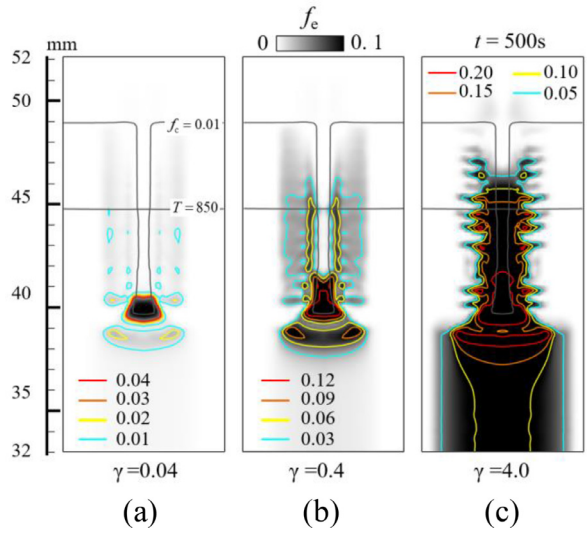

Fig. 11. Parametric study on γ of flow-driven fragmentation model. Isolines of f_e are overlaid.

6. Conclusions

Two sub-models based on capillary- and flow-driven fragmentation mechanisms were implemented in a volume-average based solidification model to investigate the formation of the as-cast structure during unidirectional solidification of the Al-7wt.%Si alloy under the RMF-induced flow condition. The experimentally determined as-cast structure and macrosegregation profiles were quantitatively reproduced by the model and the details of the solidification process of this experiment were explained. The RMF-induced primary/secondary flow led to the formation of a central segregation channel in the columnar-dominant mushy zone. Fragments as-generated near the front of columnar dendrite tips and/or around the central segregation channel were transported out of the mushy zone. Some of them were re-melted in the superheated region, whereas others continued to grow as equiaxed grains in a thin layer of the undercooled layer near the columnar tip front and were finally captured by the growing columnar dendrites in the middle-radius region of the sample.

The contributions of both fragmentation mechanisms were analysed independently. The capillary-driven fragmentation, which is rooted in the dendrite coarsening, occurs mainly in the periph-

ery region of the sample at a certain depth of the mushy zone. These fragments are hard to be transported out of the mushy zone. The flow-driven fragmentation, which is related to the interdendritic flow enhanced re-melting of dendrites, occurs mostly near the front of the mushy zone and/or around the central segregation channel. These fragments contribute mostly to the final as-cast structure. The flow-driven fragmentation mechanism is evidently dominant in this experiment. Note that the solidification time in the present experiment is rather short compared with that of 'normal' castings. Therefore, there is an extremely short time period for coarsening; hence, the weak contribution of the capillary-driven fragmentation mechanism. The current authors did a similar comparison study based on another solidification experiment with aqueous ammonium chloride solution [43]. An opposite conclusion was drawn in that study, i.e., the capillary-driven fragmentation mechanism appeared to provide a better explanation for the microstructure formation in that experiment. Therefore, both capillary- and flow-driven fragmentation mechanisms should be included in the solidification model.

As an outlook, further studies are required to validate these results. This study proposes to add both sub-models that are actually derived from two different theoretical backgrounds. Using parametric studies, fragmentation coefficients/constants were determined individually for each sub-model to balance their contributions to the final microstructure formation mechanism. A unified fragmentation sub-model that considers both capillary and flow effects is sought. Further studies are required to investigate whether the current capillary-driven fragmentation sub-model (or the coarsening law) can be extended by considering the flow effect or the flow-driven fragmentation sub-model can be extended by considering the capillary effect.

Declaration of Competing Interest

The authors declare that they have no known competing financial interests or personal relationships that could have appeared to influence the work reported in this paper.

Acknowledgements

This work was financially supported by the FWF Austrian Science Fund and the Hungarian National Research Development, and Investigation Office (No. 130946) in the framework of the FWF-NKFIN joint project (FWF, I4278-N36) and the Austria Research Promotion Agency (FFG) through the Bridge 1 project (No. 868070). The authors thank for Erzsébet Nagy and Dániel Koncz-Horváth for the EBSD investigation.

References

[1] G. Zimmermann, C. Pickmann, E. Schaberger-Zimmermann, V. Galindo, K. Eckert, S. Eckert, Do rotating magnetic fields unconditionally lead to grain refinement? A case study for directionally solidified Al-10 wt% Cu alloys, Materialia 3 (2018) 326–337, doi:10.1016/j.mtla.2018.08.036.
[2] E. Liotti, A. Lui, R. Vincent, S. Kumar, Z. Guo, T. Connolley, I.P. Dolbnya, M. Hart, L. Arnberg, R.H. Mathiesen, P.S. Grant, A synchrotron X-ray radiography study of dendrite fragmentation induced by a pulsed electromagnetic field in an Al-15Cu alloy, Acta Mater. 70 (2014) 228–239, doi:10.1016/j.actamat.2014.02.024.
[3] A. Hellawell, S. Liu, S.Z. Lu, Dendrite fragmentation and the effects of fluid flow in castings, JOM 49 (1997) 18–20, doi:10.1007/BF02914650.
[4] M.C. Flemings, Dendrite fragmentation in semisolid casting: Could we do this better? Solid State Phenom. 285 (2019) 3–11, doi:10.4028/www.scientific.net/SSP.285.3.
[5] S. Kunstreich, Electromagnetic stirring for continuous casting - Part 2, Metall. Res. Technol. 100 (2003) 1043–1061.
[6] J.A. Spittle, Columnar to equiaxed grain transition in as solidified alloys, Int. Mater. Rev. 51 (2006) 247–269, doi:10.1179/174328006X102493.
[7] M. Ghods, M. Lauer, S.R. Upadhyay, R.N. Grugel, S.N. Tewari, D.R. Poirier, Spurious grain formation at cross-sectional expansion during directional solidification: influence of thermosolutal convection, J. Mater. Eng. Perform. 27 (2018) 3122–3130, doi:10.1007/s11665-018-3364-0.
[8] J.W. Aveson, P.A. Tennant, B.J. Foss, B.A. Shollock, H.J. Stone, N. D'Souza, On the origin of sliver defects in single crystal investment castings, Acta Mater. 61 (2013) 5162–5171, doi:10.1016/j.actamat.2013.04.071.
[9] K.A. Jackson, J.D. Hunt, D.R. Uhlmann, T.P. Seward, On origin of equiaxed zone in castings, Trans. Metall. Soc. AIME 236 (1966) 149–158.
[10] M.C. Flemings, Coarsening in solidification processing, Mater. Trans. 46 (2005) 895–900, doi:10.2320/matertrans.46.895.
[11] H. Neumann-Heyme, K. Eckert, C. Beckermann, Dendrite fragmentation in alloy solidification due to sidearm pinch-off, Phys. Rev. E 92 (2015) 060401, doi:10.1103/PhysRevE.92.060401.
[12] T. Cool, P.W. Voorhees, The evolution of dendrites during coarsening: Fragmentation and morphology, Acta Mater. 127 (2017) 359–367, doi:10.1016/j.actamat.2017.01.029.
[13] C.M.G. Rodrigues, M. Wu, H. Zhang, A. Ludwig, A. Kharicha, Bridging capillary-driven fragmentation and grain transport with mixed columnar-equiaxed solidification, Metall. Mater. Trans. A 52 (2021) 4609–4622, doi:10.1007/s11661-021-06414-2.
[14] S.-C. Huang, M.E. Glicksman, Overview 12: Fundamentals of dendritic solidification—II development of sidebranch structure, Acta Metall. 29 (1981) 717–734, doi:10.1016/0001-6160(81)90116-4.
[15] G. Salloum-Abou-Jaoude, H. Nguyen-Thi, G. Reinhart, R.H. Mathiesen, G. Zimmermann, D. Voss, Characterization of motion of dendrite fragment by X-ray radiography on Earth and under microgravity environment, Mater. Sci. Forum. 790–791 (2014) 311–316, doi:10.4028/www.scientific.net/MSF.790-791.311.
[16] R.H. Mathiesen, L. Arnberg, P. Bleuet, A. Somogyi, Crystal fragmentation and columnar-to-equiaxed transitions in Al-Cu studied by Synchrotron x-ray video microscopy, Metall. Mater. Trans. A 37 (2006) 2515–2524, doi:10.1007/BF02586224.
[17] D. Ruvalcaba, R.H. Mathiesen, D.G. Eskin, L. Arnberg, L. Katgerman, In situ observations of dendritic fragmentation due to local solute-enrichment during directional solidification of an aluminum alloy, Acta Mater. 55 (2007) 4287–4292, doi:10.1016/j.actamat.2007.03.030.
[18] T. Nelson, B. Cai, N. Warnken, P.D. Lee, E. Boller, O.V. Magdysyuk, N.R. Green, Gravity effect on thermal-solutal convection during solidification revealed by four-dimensional synchrotron imaging with compositional mapping, Scr. Mater. 180 (2020) 29–33, doi:10.1016/j.scriptamat.2019.12.026.
[19] B. Cai, J. Wang, A. Kao, K. Pericleous, A.B. Phillion, R.C. Atwood, P.D. Lee, 4D synchrotron X-ray tomographic quantification of the transition from cellular to dendrite growth during directional solidification, Acta Mater. 117 (2016) 160–169, doi:10.1016/j.actamat.2016.07.002.
[20] E. Liotti, A. Lui, S. Kumar, Z. Guo, C. Bi, T. Connolley, P.S. Grant, The spatial and temporal distribution of dendrite fragmentation in solidifying Al-Cu alloys under different conditions, Acta Mater 121 (2016) 384–395, doi:10.1016/j.actamat.2016.09.013.
[21] N. Limodin, L. Salvo, E. Boller, M. Suéry, M. Felberbaum, S. Gailliègue, K. Madi, In situ and real-time 3-D microtomography investigation of dendritic solidification in an Al–10 wt% Cu alloy, Acta Mater. 57 (2009) 2300–2310, doi:10.1016/j.actamat.2009.01.035.
[22] Z. Zhang, C. Wang, B. Koe, C.M. Schlepütz, S. Irvine, J. Mi, Synchrotron X-ray imaging and ultrafast tomography in situ study of the fragmentation and growth dynamics of dendritic microstructures in solidification under ultrasound, Acta Mater. 209 (2021) 116796, doi:10.1016/j.actamat.2021.116796.
[23] N. Shevchenko, O. Roshchupkina, O. Sokolova, S. Eckert, The effect of natural and forced melt convection on dendritic solidification in Ga-In alloys, J. Cryst. Growth 417 (2015) 1–8, doi:10.1016/j.jcrysgro.2014.11.043.
[24] B. Chalmers, R.B. Williamson, Crystal multiplication without nucleation, Science 148 (1965) 1717–1718, doi:10.1126/science.148.3678.1717.
[25] A.M. Mullis, D.J. Walker, S.E. Battersby, R.F. Cochrane, Deformation of dendrites by fluid flow during rapid solidification, Mater. Sci. Eng. A 304 (2001) 245–249, doi:10.1016/S0921-5093(00)01477-5.
[26] C.J. Paradies, R.N. Smith, M.E. Glicksman, The influence of convection during solidification on fragmentation of the mushy zone of a model alloy, Metall. Mater. Trans. A. 28 (1997) 875–883, doi:10.1007/s11661-997-1016-3.
[27] J. Pilling, A. Hellawell, Mechanical deformation of dendrites by fluid flow, Metall. Mater. Trans. A 27 (1996) 229–232, doi:10.1007/BF02647763.
[28] H. Neumann-Heyme, K. Eckert, C. Beckermann, General evolution equation for the specific interface area of dendrites during alloy solidification, Acta Mater 140 (2017) 87–96, doi:10.1016/j.actamat.2017.08.021.
[29] N. Ren, C. Panwisawas, J. Li, M. Xia, H. Dong, J. Li, Solute enrichment induced dendritic fragmentation in directional solidification of nickel-based superalloys, Acta Mater. 215 (2021) 117043, doi:10.1016/j.actamat.2021.117043.
[30] T. Takaki, M. Ohno, T. Shimokawabe, T. Aoki, Two-dimensional phase-field simulations of dendrite competitive growth during the directional solidification of a binary alloy bicrystal, Acta Mater. 81 (2014) 272–283, doi:10.1016/j.actamat.2014.08.035.
[31] M. Wu, A. Ludwig, Modeling equiaxed solidification with melt convection and grain sedimentation-I: model description, Acta Mater 57 (2009) 5621–5631, doi:10.1016/j.actamat.2009.07.056.
[32] M. Wu, A. Ludwig, Using a three-phase deterministic model for the columnar-to-equiaxed transition, Metall. Mater. Trans. A 38 A (2007) 1465–1475, doi:10.1007/s11661-007-9175-9.
[33] C.Y. Wang, C. Beckermann, Equiaxed dendritic solidification with convection: Part I. Multiscale/multiphase modeling, Metall. Mater. Trans. A 27 (1996) 2754–2764, doi:10.1007/BF02652369.

[34] J.P. Gu, C. Beckermann, A.F. Giamei, Motion and remelting of dendrite fragments during directional solidification of a nickel-base superalloy, Metall. Mater. Trans. A 28 (1997) 1533–1542, doi:10.1007/s11661-997-0215-2.
[35] M. Wu, A. Ludwig, A. Kharicha, Volume-averaged modeling of multiphase flow phenomena during alloy solidification, Metals (Basel) 9 (2019) 229, doi:10.3390/met9020229.
[36] G. Lesoult, Macrosegregation in steel strands and ingots: Characterisation, formation and consequences, Mater. Sci. Eng. A 413–414 (2005) 19–29, doi:10.1016/j.msea.2005.08.203.
[37] N. Leriche, H. Combeau, C.-A. Gandin, M. Založnik, Modelling of columnar-to-equiaxed and equiaxed-to- columnar transitions in ingots using a multiphase model, IOP Conf. Ser. Mater. Sci. Eng. 84 (2015) 012087, doi:10.1088/1757-899X/84/1/012087.
[38] G.E.Nereo M.C.Flemings, Macrosegregation: part I, Trans. Metall. Soc. AIME 239 (1967) 1449–1462.
[39] T. Campanella, C. Charbon, M. Rappaz, Grain refinement induced by electromagnetic stirring: a dendrite fragmentation criterion, Metall. Mater. Trans. A 35 (2004) 3201–3210, doi:10.1007/s11661-004-0064-1.
[40] Y. Zheng, M. Wu, A. Kharicha, A. Ludwig, Incorporation of fragmentation into a volume average solidification model, Model. Simul. Mater. Sci. Eng. 26 (2018) 015004, doi:10.1088/1361-651X/aa86c5.
[41] Y. Zheng, M. Wu, E. Karimi-Sibaki, A. Kharicha, A. Ludwig, Use of a mixed columnar-equiaxed solidification model to analyse the formation of as-cast structure and macrosegregation in a Sn-10 wt% Pb benchmark experiment, Int. J. Heat Mass Transf. 122 (2018) 939–953, doi:10.1016/j.ijheatmasstransfer.2018.02.012.
[42] Z. Zhang, M. Wu, H. Zhang, S. Hahn, F. Wimmer, A. Ludwig, A. Kharicha, Modeling of the as-cast structure and macrosegregation in the continuous casting of a steel billet: Effect of M-EMS, J. Mater. Process. Technol. 301 (2022) 117434, doi:10.1016/j.jmatprotec.2021.117434.
[43] C.M.G. Rodrigues, M. Wu, H. Zhang, A. Ludwig, A. Kharicha, Validation of a capillary-driven fragmentation model dur-ing mixed columnar-equiaxed solidification with melt con-vection and grain transport, Materialia 23 (2022) 101462, doi:10.1016/j.mtla.2022.101462.
[44] Z. Veres, A. Roósz, A. Rónaföldi, A. Sycheva, M. Svéda, The effect of melt flow induced by RMF on the meso- and micro-structure of unidirectionally solidified Al–7wt.% Si alloy Benchmark experiment under magnetic stirring, J. Mater. Sci. Technol. 103 (2022) 197–208, doi:10.1016/j.jmst.2021.06.060.
[45] J. Lipton, M.E. Glicksman, W. Kurz, Dendritic growth into undercooled alloy metals, Mater. Sci. Eng. 65 (1984) 57–63, doi:10.1016/0025-5416(84)90199-X.
[46] H. Zhang, M. Wu, P. Schumacher, C.M.G. Rodrigues, A. Ludwig, A. Kharicha, Modelling melting and grain destruction phenomena during globular equiaxed solidification, Appl. Math. Model. 97 (2021) 821–838, doi:10.1016/j.apm.2021.04.024.
[47] C. Beckermann, Modeling segregation and grain structure development in equiaxed solidification with convection, JOM 49 (1997) 13–17, doi:10.1007/BF02914649.
[48] Q. Li, C. Beckermann, Scaling behavior of three-dimensional dendrites, Phys. Rev. E. 57 (1998) 3176–3188, doi:10.1103/PhysRevE.57.3176.
[49] P.N. Rowe, Heat and mass transfer from a single sphere to fluid flowing through an array, Trans. Inst. Chem. Eng. 43 (1965) 321–331.
[50] M. Wu, A. Ludwig, A three-phase model for mixed columnar-equiaxed solidification, Metall. Mater. Trans. A 37 (2006) 1613–1631, doi:10.1007/s11661-006-0104-0.
[51] J.K. Roplekar, J.A. Dantzig, Int. J. Cast Met. Res. 14 (2001) 79–95, doi:10.1080/13640461.2001.11819428.
[52] H. Zhang, M. Wu, C.M.G. Rodrigues, A. Ludwig, A. Kharicha, Directional solidification of AlSi7Fe1 alloy under forced flow conditions: effect of intermetallic phase precipitation and dendrite coarsening, Metall. Mater. Trans. A. 52 (2021) 3007–3022, doi:10.1007/s11661-021-06295-5.
[53] T. Cool, P.W. Voorhees, Dendrite fragmentation: an experiment-driven simulation, Philos. Trans. R. Soc. A Math. Phys. Eng. Sci. 376 (2018) 20170213, doi:10.1098/rsta.2017.0213.
[54] H. Zhang, M. Wu, Y. Zheng, A. Ludwig, A. Kharicha, Numerical study of the role of mush permeability in the solidifying mushy zone under forced convection, Mater. Today Commun. 22 (2020) 100842, doi:10.1016/j.mtcomm.2019.100842.
[55] J.W. Gao, C.Y. Wang, An experimental investigation into the effects of grain transport on columnar to equiaxed transition during dendritic alloy solidification, J. Heat Transfer. 121 (1999) 430–437, doi:10.1115/1.2825996.
[56] G. Zimmermann, C. Pickmann, M. Hamacher, E. Schaberger-Zimmermann, H. Neumann-Heyme, K. Eckert, S. Eckert, Fragmentation-driven grain refinement in directional solidification of AlCu10wt-% alloy at low pulling speeds, Acta Mater. 126 (2017) 236–250, doi:10.1016/j.actamat.2016.12.063.
[57] S. Akamatsu, H. Nguyen-Thi, In situ observation of solidification patterns in diffusive conditions, Acta Mater 108 (2016) 325–346, doi:10.1016/j.actamat.2016.01.024.
[58] R.H. Mathiesen, L. Arnberg, X-ray radiography observations of columnar dendritic growth and constitutional undercooling in an Al-30 wt% Cu alloy, Acta Mater. 53 (2005) 947–956, doi:10.1016/j.actamat.2004.10.050.
[59] F. Li, J. Zhang, Q. Dong, Y. Dai, Y. Fu, H. Xie, J. Mi, F. Yin, B. Sun, In situ synchrotron X-ray studies of the coupled effects of thermal and solutal supercoolings on the instability of dendrite growth, Mater. Charact. 109 (2015) 9–18, doi:10.1016/j.matchar.2015.09.008.
[60] H. Yasuda, K. Morishita, N. Nakatsuka, T. Nishimura, M. Yoshiya, A. Sugiyama, K. Uesugi, A. Takeuchi, Dendrite fragmentation induced by massive-like δ–γ transformation in Fe–C alloys, Nat. Commun. 10 (2019) 3183, doi:10.1038/s41467-019-11079-y.
[61] H. Neumann-Heyme, N. Shevchenko, Z. Lei, K. Eckert, O. Keplinger, J. Grenzer, C. Beckermann, S. Eckert, Coarsening evolution of dendritic sidearms: From synchrotron experiments to quantitative modeling, Acta Mater 146 (2018) 176–186, doi:10.1016/j.actamat.2017.12.056.
[62] P. Bouissou, P. Pelcé, Effect of a forced flow on dendritic growth, Phys. Rev. A 40 (1989) 6673–6680, doi:10.1103/PhysRevA.40.6673.
[63] P. Bouissou, B. Perrin, P. Tabeling, Influence of an external flow on dendritic crystal growth, Phys. Rev. A 40 (1989) 509–510, doi:10.1103/PhysRevA.40.509.
[64] Q. Li, C. Beckermann, Modeling of free dendritic growth of succinonitrile-acetone alloys with thermosolutal melt convection, J. Cryst. Growth. 236 (2002) 482–498, doi:10.1016/S0022-0248(01)02390-9.